

Multi-platform Observations Characterizing the Afternoon-to-Evening Transition of the Planetary Boundary Layer in Northern Alabama, USA

Stephanie M. Wingo · Kevin R. Knupp

Received: 29 May 2014 / Accepted: 25 November 2014 / Published online: 9 December 2014
© The Author(s) 2014. This article is published with open access at Springerlink.com

Abstract Observations from the University of Alabama in Huntsville campus and ground-based scanning radar for over 140 total spring, summer, and autumn cases are studied to contribute to the relative scarcity of long-term datasets documenting the afternoon-to-evening transition of the planetary boundary layer. A sunset relative frame of reference is employed, focusing on the period 3 h before to 2 h after astronomical sunset, and several findings are consistent with previous investigations. Fluctuating components of wind and temperature computed from nearly collocated surface, Doppler wind profiler, and vertically pointing Doppler lidar measurements show a consistent decline as turbulence intensity diminishes through the transition. When normalized by their initial values, a pattern emerges: temperature variances decline slowly at first then quite abruptly after about 90 min before sunset. After the temperature variances begin to wane, vertical velocity fluctuations decrease, and the rate of their decay increases as vigorous thermal structures diminish. The fastest decline of the horizontal wind variance occurs after an accelerated vertical wind variance decrease, and the horizontal wind fluctuations display the slowest rate of decrease among these quantities. Near-surface humidity measurements show increases in mean water vapour mixing ratio as a steady rise generally beginning about 80 min prior to sunset. Composites of mean lidar vertical motion show final convective-type towers of upward motion occur about an hour before sunset and are coherent through 800 m (all heights a.g.l.). Lidar vertical motion variance at 195 m decreases by more than an order of magnitude approaching sunset, then remains below $0.01 \text{ m}^2 \text{ s}^{-2}$ for the rest of the studied time frame. Subtle, but steady, increases in both horizontal wind speed and radar-derived horizontal wind convergence above the surface layer (at 300 m) span the entire 5-h time frame. While the convergence results show a broad range, an increase in the mean is clear and found to be statistically significant. Implications

Electronic supplementary material The online version of this article (doi:[10.1007/s10546-014-9988-1](https://doi.org/10.1007/s10546-014-9988-1)) contains supplementary material, which is available to authorized users.

S. M. Wingo (✉) · K. R. Knupp
Severe Weather Institute and Radar & Lightning Laboratories (SWIRLL), Department of Atmospheric Science, University of Alabama in Huntsville, Huntsville, USA
e-mail: mullins@nsstc.uah.edu

for possible transition-effect enhancements to pre-existing low-level convergence areas are briefly noted.

Keywords Afternoon-to-evening transition · Afternoon transition · Atmospheric surface layer · Convective boundary-layer decay · Early evening transition · Multi-platform observations

1 Introduction

The planetary boundary layer (PBL) over land displays distinct daytime and nighttime structures. A well-developed daytime convective PBL is generally well mixed, dominated by buoyant thermal eddies resulting from an upward sensible heat flux. The nocturnal boundary layer is typically much shallower, stably stratified, and is often topped by a low-level jet. These two regimes have been well documented for fully the developed PBL, but specific properties and processes related to the evolution from one to the other have received relatively little attention, particularly over heterogeneous terrain. Studies published over the last several years have shown a renewed interest in the transitional PBL, with the bulk of this work focused on numerical simulation. General characteristics of the afternoon-to-evening transition (AET) time frame have been identified over many decades from surface data (Caughey et al. 1979; Mahrt 1981; Grant 1997), Doppler wind profilers (Grimsdell and Angevine 2002; Angevine 2008), sodar (Busse and Knupp 2012), and an array of numerical simulation studies (e.g. Nieuwstadt and Brost 1986; Sorbjan 1997; Pino et al. 2006; Nadeau et al. 2011). However, a refined understanding of the PBL's diurnal evolution, especially of the AET, remains an elusive problem. As a result, current PBL parametrization methods struggle to accurately reproduce observations in the hours just before and after sunset (Edwards et al. 2006; Beare et al. 2006; Holtslag et al. 2013). Observational study has become a priority, prompting the investigation presented here as well as a substantial field campaign in southern France (Lothon et al. 2014).

Boundary-layer AET events are best observed under clear sky and light wind (generally, wind speed $< 5 \text{ m s}^{-1}$) conditions (Acevedo and Fitzjarrald 2001). Under such circumstances, a variety of AET signatures have been observed. Decreases in the variance and magnitude of the near-surface wind speed and temperature have been noted in nearly all AET observational studies. Reductions in the surface heat flux lead to less vertical mixing, and the resulting decrease in turbulence is evident in this characteristic decrease. Continued evaporation near the surface as the depth of the mixed layer rapidly declines creates an increase in surface humidity that has been noted by several investigators (Fitzjarrald and Lala 1989; Acevedo and Fitzjarrald 2001; Busse and Knupp 2012; Bonin et al. 2013). Once the surface heat flux has reversed signs, it is common for a temperature inversion to develop, primarily as a result of radiational cooling. The initial stages of inversion formation can be seen as a sign reversal in a vertical temperature gradient in the surface layer. A distinct minimum in sodar acoustic backscatter (which is dependant on the temperature structure parameter), coincident with a relative minimum in the vertical extent of sodar returns at about the time of sunset, has been shown to result from decreased temperature fluctuations (Busse and Knupp 2012). Further, a decrease in the vertical extent and vigour of daytime PBL thermals measured by wind profilers has been noted as an early indication of the afternoon-to-evening transition (Grimsdell and Angevine 2002; Angevine 2008). Each of these AET signatures has been shown to occur at various sunset relative times, in an often inconsistent order, and can vary from location to location and day to day.

Implications of a full understanding of the AET period include the accurate forecasting of, not only nighttime minimum temperature, but also the formation of fog or frost and the concentration of pollutants into the evening and overnight hours. These important applications can affect industries including agriculture, forest management (controlled burns), transportation safety, and public health. The evolution of momentum transfer and the distribution of thermodynamic quantities within the residual layer, as well as impacts on the development of the preceding day's PBL (e.g. [Bennett et al. 2010](#)), represent further questions that may hinge on the PBL's AET behaviour. Additionally, some studies have indicated that PBL processes during the AET time frame can affect the vigour of existing convection or the initiation of new clouds or storms. [Bluestein \(2008\)](#) noted the common delay in convective initiation along southern USA Plains drylines until near sunset, coining the term "6:00 magic." Simulations described by [Jones and Bannon \(2002\)](#) show that the location and propagation of drylines in the southern Plains are highly dependent on the magnitude and changes of the surface heat flux, with a peak in inversion height and increase in low-level convergence ahead of the boundary occurring at sunset. Analysis by [Murphey et al. \(2006\)](#) presents an example of dryline convective initiation triggered by enhanced low-level convergence in the AET period. Numerical models have struggled to accurately capture the daily cycle of the PBL (e.g. [Holtslag et al. 2013](#)), and improving existing parametrizations will first require more complete observations and a better understanding of the PBL's diurnal transitions.

[Caughey et al. \(1979\)](#) and [Mahrt \(1981\)](#) led early observational studies, but long term, multi-platform datasets documenting the afternoon-to-evening transition have remained scarce in comparison to records of the fully developed daytime and nighttime PBL. Recent work by [Busse and Knupp \(2012\)](#), [Bonin et al. \(2013\)](#), and a large field study in southern France ([Lothon et al. 2014](#)) have begun to address this relative paucity of AET observations; the current effort is presented to bolster this growing body of work. With an array of significant applications, we aim to characterize multi-season, clear-air PBL changes observed by a variety of platforms during the AET period and assess any potential implications for convective initiation or enhancement. In this context, our working hypothesis includes the notion that decreased near-surface wind speeds occur in the AET while the wind speed above the surface layer increases in response to the waning surface heat flux and associated reductions in turbulent kinetic energy (TKE) and vertical momentum transport. When an existing area of horizontal convergence is in place (e.g. along a boundary) above the surface layer, our hypothesis implies this convergence will increase during the transition. Consistent with the inertial oscillation, flow acceleration above the surface layer would support, by continuity, an enhancement in any existing convergence at that height and suggest a possible convective initiation or enhancement signal. The following sections give an overview of the measurement platforms and analysis methods employed, results including seasonal variations and discussion, and finally conclusions regarding the clear air AET period in Huntsville, Alabama, USA, are noted.

2 Data and Analysis Methods

Observations were collected as part of the Atmospheric Boundary Identification and Delineation Experiment (ABIDE) field project on the campus of the University of Alabama in Huntsville (UAH) during the spring to autumn period (March–November) of 2012 and 2013. To facilitate our multi-platform approach, measurements included are from standard surface instrumentation, ground-based scanning radar, the UAH Mobile Integrated Profiling System (MIPS), and the recently acquired UAH Doppler wind lidar (DWL). Table 1 lists brief

Table 1 Platform descriptions and measurement characteristics

Instrument	Description	Quantities measured or calculated	Measurement height	Spatial resolution	Temporal resolution
MIPS Doppler wind profiler (915 DWPF)	33 cm wavelength, 9° beam width, zenith and off-zenith beams (3–5 depending on mode) for wind profile retrieval	Signal-to-noise ratio (C_n^2), vertical motion, Doppler spectra and width, horizontal wind profile	0.19–4 km	60 or 106 m, depending on mode	60 s (19 s or 30 s dwell time, depending on mode)
MIPS Ceilometer	0.905 μm wavelength	Total path (2-way) aerosol backscatter, cloud base height	0.3–10+ km depending on conditions	30 m gate length	15 s
MIPS Microwave profiling radiometer (MPR)	Seven channels between 51–19 GHz, 5 channels between 21–30 GHz	Temperature, water vapor mixing ratio, integrated water vapor, and integrated cloud water profiles	Surface–10 km	100 m up to 1 km, 250 m above 1 km	1–14 min (1 min in this study)
Doppler wind lidar (DWL)	1.5 μm wavelength, heterodyne detection	Vertical motion, signal-to-noise ratio, attenuated aerosol backscatter (β)	75–1,000 m	selectable gate length from 22.5 m (30 m in this study)	1–10 Hz (2 Hz in this study)
ARMOR radar	5.36 cm (C-band), 1200 Hz PRF, 1.0° beam width, dual-polarization (STAR)	Reflectivity, radial velocity, spectrum width, differential reflectivity (Z_{DR}), correlation coefficient (ρ_{HV}), differential phase (Φ_{DP})	3 (up to 2.0°) or 5 (up to 3.4°) tilt volumes, first gate at 1 km range	250 m gate length	2–5 min volume update
Surface		Temperature, relative humidity, pressure, wind speed, wind direction, solar radiation	2 m, with temperature and winds also at 10 m	n/a	Recorded at 1-s or 5-s interval

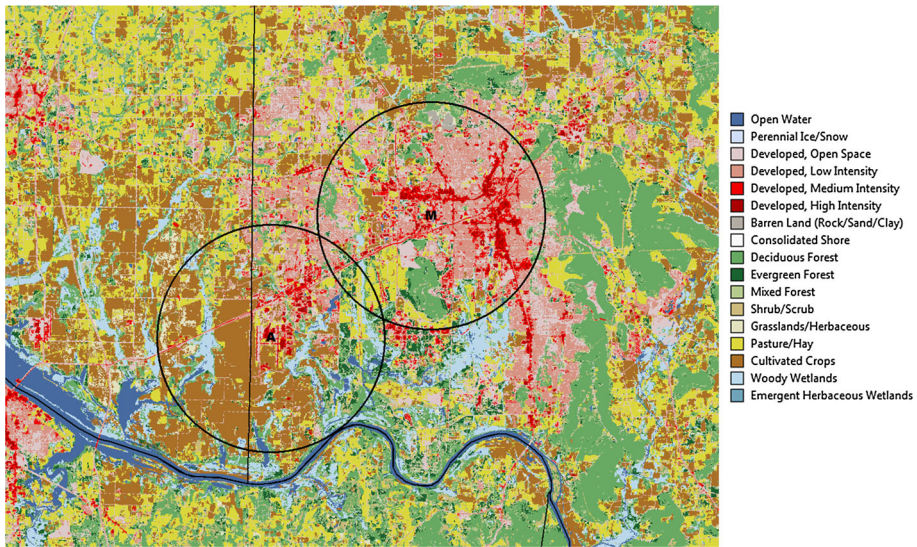


Fig. 1 Study region land-cover classifications (colours, legend at right) as described in the USGS National Land Cover Database (Fry et al. 2011). “M” indicates the MIPS location at UAH, “A” shows the location of the ARMOR radar at the Huntsville International Airport; 10 km radius circles are drawn about each. Other solid black lines indicate county boundaries

descriptions and specifications of each instrument. The MIPS includes a 915-MHz Doppler wind profiler (915 DWP), a 12-channel microwave profiling radiometer (MPR), and a Vaisala laser ceilometer (Karan and Knupp 2006; Knupp et al. 2009; Busse and Knupp 2012). For the cases considered herein, the MIPS was located at the UAH campus within an earthen berm enclosure. In the spring of 2013, UAH acquired the scanning-capable 1.5 μm DWL, which operated in vertical stare mode from a laboratory atop a building near the MIPS berm (equating to about 145 m separation distance between these platforms) for the considered cases. Figure 1 portrays the various land-surface types in the vicinity of the study location.

Here, we define “clear air” days as those when total sky cloud cover is minimal, i.e., days with cumulus cloud cover less than about 20–30%. Cases are required to have minimal large-scale forcing, so case days are generally similar on the synoptic scale with high pressure over northern Alabama and the south-eastern USA, low mean surface wind speeds ($<5\text{ m s}^{-1}$), and clear, or at most scattered, cloud cover. We assume temporal cloud coverage is representative of areal cloud cover, and diagnose the coverage using the MIPS ceilometer and surface pyranometer. While substantial effort is made to ensure all data platforms are continuously operational, there are instances when not all platforms are available. Also, because it was newly acquired in 2013, the DWL is available only for some of the 2013 cases. Table 2 summarizes the available data platforms for each seasonal group studied. Busse and Knupp (2012) showed that the average time of many AET indicators for summer and autumn days at the same observation site can range from more than 2 h before sunset to over 1 h after sunset. Following their findings, this study of a larger number of events uses a set time range of 3 h before to 2 h after sunset as the general AET time interval.

Measurements of the 2-m and 10-m (all heights are a.g.l.) temperature (T_2 , T_{10} , respectively) and 10-m horizontal wind components (u_{10} , v_{10} , eastward and northward components, respectively) are used to evaluate changes in variances of each variable, as well as the vertical

Table 2 Data availability for each case group by season: spring (March–May), summer (June–August), and autumn (September–November)

	Total cases	Cases with data platform available					
		Surface	MIPS Ceilometer	MIPS 915 DWP	MIPS MPR	ARMOR	DWL
2012							
Spring	20	20	16	17	13	19	–
Summer	22	20	21	5	16	18	–
Autumn	15	15	15	8	8	14	–
Mar–Nov	57	55	52	30	37	51	–
2013							
Spring	26	26	24	11	23	9	–
Summer	28	27	28	27	21	14	16
Autumn	32	32	32	27	30	28	14
Mar–Nov	86	85	84	65	74	51	30
2012–2013							
Spring	46	46	40	28	36	28	–
Summer	50	47	49	32	37	32	16
Autumn	47	47	47	35	38	42	14
Mar–Nov	143	140	136	95	111	102	30

temperature difference ($T_2 - T_{10}$).¹ These quantities represent simple indicators of the transition: decreases in the variances suggest less turbulent PBL motions, and often a change of sign for $T_2 - T_{10}$ occurs indicating early inversion formation. Temperature data are recorded with a Vaisala HMP45-C sensor at 2-m height and with a Campbell Scientific 107 sensor at 10-m height. The former has a specified response time of 15 s for humidity at 20 °C in still air, and the latter a temperature response time of up to 60 s for a wind speed of 5 m s⁻¹. These sensors are ventilated, but not aspirated, so in practice their response times for the temperature measurements used herein likely exceed the specified values. Due to the longer practical response times of these instruments, our computed variances are attenuated values of the true turbulent fluctuations. Still, as will be shown, analysis of the computed variances yields similar trends as previous work. For cases from August to November 2012, surface data are recorded at a 1-s interval, but due to intermittent power supply issues, some cases contain gaps when data were not recorded. If 20% or more data in the 5-h AET interval are missing, the case is not included. Surface data are recorded at a consistent 5-s interval for all other cases (March–July 2012, and March–November 2013). For August–November 2012 cases, the 1-s data are first averaged to a 5-s interval. Once all cases have a consistent temporal interval, variances are computed about a 15-min mean. Wind components (u_{10} and v_{10}) are combined to arrive at the total horizontal wind variance, $\overline{U^2}$, which can be viewed as an analogue for the horizontal component of TKE. Surface data are available for 140 of the 143 total cases in this study (Table 2).

¹ This approach is consistent with first-order closure in which the vertical heat flux is approximated by $\overline{w'\theta'} = -K_H (\partial\bar{\theta}/\partial z)$, where K_H is the eddy heat diffusivity, which for a neutral surface layer can be parametrized as the product of mixing length and the vertical gradient of the mean wind, i.e., $l^2 |\partial\bar{U}/\partial z|$ (Stull 1988).

Because the decrease in surface heat flux is associated with a decline in the vertical momentum transport and decay of large PBL eddies (e.g. Angevine 2008), vertical motion variance should also exhibit a marked decline during the afternoon-to-evening transition. Simulations by Nieuwstadt and Brost (1986), Pino et al. (2006), and Nadeau et al. (2011) all indicate a faster rate of decline in vertical than in horizontal velocity fluctuations. Profiles of vertical motion are obtained from the 915 DWP and DWL. These data are used to compute the mean and variance of vertical motion. Vertical motion data from the 915 DWP are recorded on average at an interval of 39 s (depending on operation mode), and the DWL employs a temporal resolution of 2 Hz. Vertical gate spacing for the 915 DWP is either 60 or 106 m (depending on operation mode), and each sample represents a 19-s or 30-s average, again depending on the operation mode. The 30-m DWL vertical gate spacing for this study did not vary among the cases, nor did the number of pulse integrations (5,000) used in the sampling. Vertical motion variances from each platform are computed using a 15-min mean. It is important to recall that the vertical motion detected by the 915 DWP is really a combination of air motion and the motion of any particulate scatterers present in the radar beam. Several studies have noted a bias due to presumably biological targets (e.g. Wilson et al. 1994; Angevine 1997). Velocity measurements from the DWL, which rely on heterodyne detection at a much shorter wavelength and a very stable transceiver, are quite insensitive to velocity contamination common to radar platforms (Pearson et al. 2009). Data from the 915 DWP are available for 95 of the 143 total cases, and the DWL provided observations for 30 cases in the summer and autumn of 2013. The 915 DWP is also quality controlled by applying the Weber-Wuertz intermittent clutter rejection algorithm outlined by Bianco et al. (2013). Additionally, profiles of horizontal wind from the 915 DWP are obtained by applying the NCAR Improved Moments Algorithm (NIMA; Cornman et al. 1998; Morse et al. 2002) at 10-min intervals to remove spectral contamination and derive consensus wind components. These profiles (available for 89 cases) are used to assess horizontal wind magnitude changes.

Due to continuing evaporation as vertical mixing decreases, it is usual for the surface water vapour mixing ratio (r_v) to increase throughout the AET time frame (Fitzjarrald and Lala 1989; Acevedo and Fitzjarrald 2001; Busse and Knupp 2012; Bonin et al. 2013). Such characteristic behaviour is considered here using the MIPS MPR. The MPR r_v data are used in favour of the surface data because the MPR did not experience power supply issues resulting in gaps in the record for any given case. Surface (2 m) r_v values are recorded at 1-min resolution, and a 15-min moving average is applied across the 5-h AET interval for all cases. To evaluate trends among the groups of cases, differences in mean r_v from the value at the start of the AET interval (3 h prior to sunset) are obtained. Additionally, mean r_v values normalized by the initial value are also computed to further facilitate comparison at each sunset relative time. MPR data are available for 111 of the 143 total cases.

Observations from the Advanced Radar for Meteorological and Operational Research (ARMOR) are used in an attempt to broaden the study beyond point and profile measurements. ARMOR is a C-band dual-polarimetric Doppler radar located at the Huntsville International Airport, about 15 km south-west of the UAH campus (see Fig. 1). Selected parameters of the radar are included in Table 1, and further specifications and details on ARMOR can be found in Petersen et al. (2009). For the cases of interest here, ARMOR operated in a routine pattern of low-level 360° scans at elevation angles of 0.7°, 1.3°, 2.0°, 2.7°, and 3.4° with a varied cycle update time of 2–5 min. Cases prior to 12 June 2013 contain only the first three elevations. Editing to remove ground targets and any possible range or velocity aliasing is completed with NCAR's Solo II software (Oye et al. 1995). Estimates of meso- γ scale convergence are obtained by applying the Extended Velocity-Azimuth Display (EVAD) analysis technique (Matejka and Srivastava 1991) using a 10-km radius for analysis circles

(Fig. 1). This is completed with NCAR's RadX software (Dixon 2010). ARMOR data are not included for events with limited clear air return (less than 60% areal coverage within 20-km range of the radar) at the start of the 5-h study interval. With this stipulation, ARMOR data are available for 102 of the 140 total cases in this study. Missing days are either due to very low clear air return (primarily in March and November), or times when ARMOR was not operational.

The investigated quantities described above are placed in a common reference frame by converting the UTC time coordinate to sunset relative time. For each case group shown in Table 2, the range of values for each of these quantities is determined. Mean values at each sunset relative time are computed, as well as a total percent change across the 5-h time frame for each field (see Table S1 in the Supplementary material). Additionally, a quartile analysis of each quantity is made at 20-min interval sunset relative time bins to show the evolution of the range of values for each parameter throughout the AET period. Finally, each variance quantity is averaged among all cases and normalized by the 3-h pre-sunset values to permit a comparison of the relative timing at which these parameters decay.

3 Results and Discussion

Table 2 shows data platform availability by season, and Table S1 presents an overview of mean values for selected parameters at each sunset relative time bin. Further details on results for each quantity studied are described below.

3.1 Surface Data

Mean values of $\overline{U'^2}$ in sunset relative time are shown in Fig. 2a. A systematic decrease in $\overline{U'^2}$ occurs during the AET period for all cases. Spring transitions generally begin with a higher $\overline{U'^2}$ and autumn events with a lower $\overline{U'^2}$. Spring events exhibit an initial $\overline{U'^2}$ decrease starting on average about 145 min before sunset, and at about 85 min pre-sunset the decline is sharper. By about 30 min after sunset, the mean $\overline{U'^2}$ of spring cases is steady. This quasi step-like behaviour is also seen in the summer events, with a faster rate of $\overline{U'^2}$ decline after 135 min pre-sunset, and is in line with Busse and Knupp (2012), who identified a step-like shape in surface wind speed and temperature values in some of their 30 AET events at the same location. In autumn, $\overline{U'^2}$ is generally smaller than in the other seasons, and the more rapid decline begins about 80 min pre-sunset, about 1 h later than the accelerated decline seen in the summer cases. After sunset, the seasons show less variation as a generally steady mean value is achieved, slightly higher in spring and summer than in autumn. When the $\overline{U'^2}$ values are normalized by the value at the start of the time frame (Fig. 2b), the seasons are more closely similar, though the step-like pattern is still notable, especially in spring.

A recent numerical study by Nadeau et al. (2011) considers the transition as consecutive sub-periods with different rates of TKE decay. Our observations show a pattern consistent with that framework. An analogue for TKE, $\overline{U'^2}$, exhibits a faster decline after about 100 min pre-sunset than before, and as will be shown later, the variance of vertical motions declines even faster. We interpret this as a reflection of the decrease in buoyant vertical motions as the surface heat flux decreases, and as a result there is less turbulent transport of momentum in the vertical, prompting an acceleration in the rate of decline of the horizontal wind fluctuations. The rate of $\overline{U'^2}$ decline increases in all seasons, but the time of the increased decline varies. Equinox seasons show a faster $\overline{U'^2}$ decrease starting on average 80 min prior to sunset, while

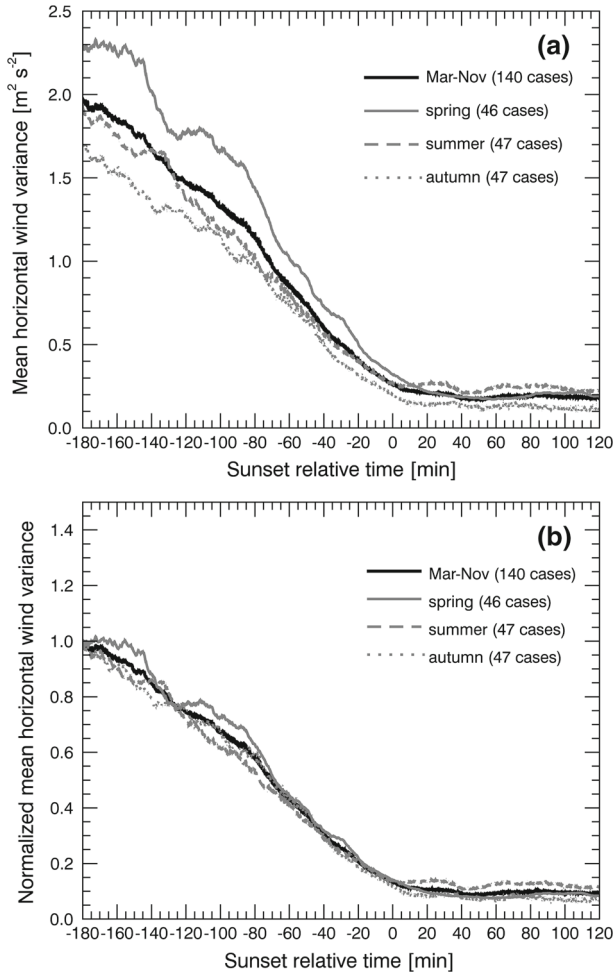


Fig. 2 Mean variance **a** of 10-m horizontal wind for all available cases (*bold black curve*) and by season (*grey curves*) in sunset relative time; **b** the same, normalized by value at 3 h before sunset

in summer it begins about 1 h earlier. A similar effect is noted in [Nadeau et al. \(2011\)](#), who found a more rapid TKE decay rate in their early evening sub-period (defined as when the surface sensible heat flux first reaches a negative value) than during their afternoon sub-period (defined as the interval of decreasing heat flux).

The spread of $\overline{U'^2}$ values among the cases is presented in a quartile analysis in [Fig. 3](#). Overall, $\overline{U'^2}$ at the end of the AET period (2 h after sunset) is roughly an order of magnitude less than at the start (3 h before sunset, [Table S1](#)). However, there is considerably more spread among individual cases post-sunset. For each sunset relative time bin, cases with $\overline{U'^2}$ values beyond 1.5 times greater than the inner quartile range are plotted as outliers (small circles). In all seasons, the range of $\overline{U'^2}$ values decreases leading up to sunset, with spring (autumn) cases having the largest (smallest) initial values. The trend in the range is similar in all seasons; this is particularly clear in a quartile analysis of normalized $\overline{U'^2}$ values (see [Fig. S1](#) in the Supplementary material).

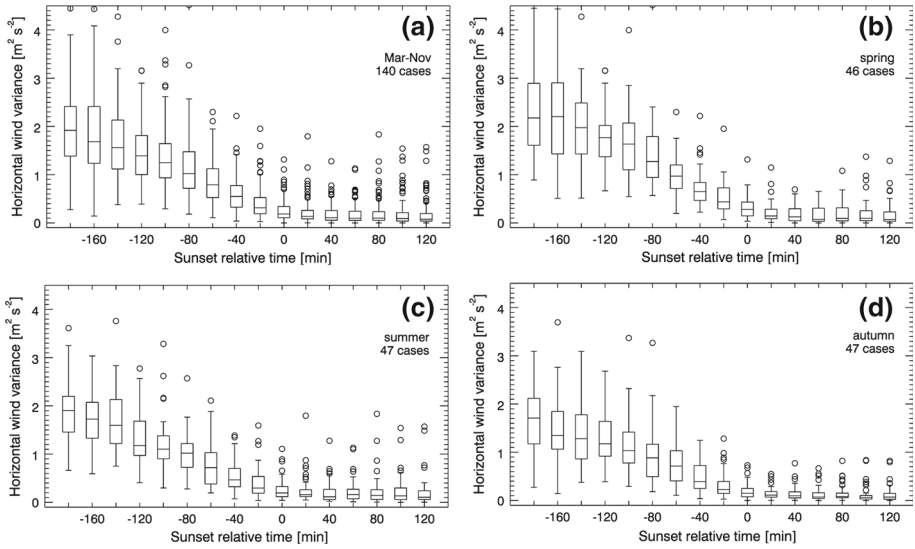


Fig. 3 Quartile analysis of 10-m horizontal wind variance for all available cases **a** and by season **b–d** for 20-min interval sunset relative time bins. The *middle line of each box* shows the median value, while the *bottom and top lines of the boxes* show the 25th and 75th percentile values, respectively. *Whiskers* show maximum and minimum values within $1.5\times$ the inner quartile range, and outliers beyond this range are plotted as *circles*

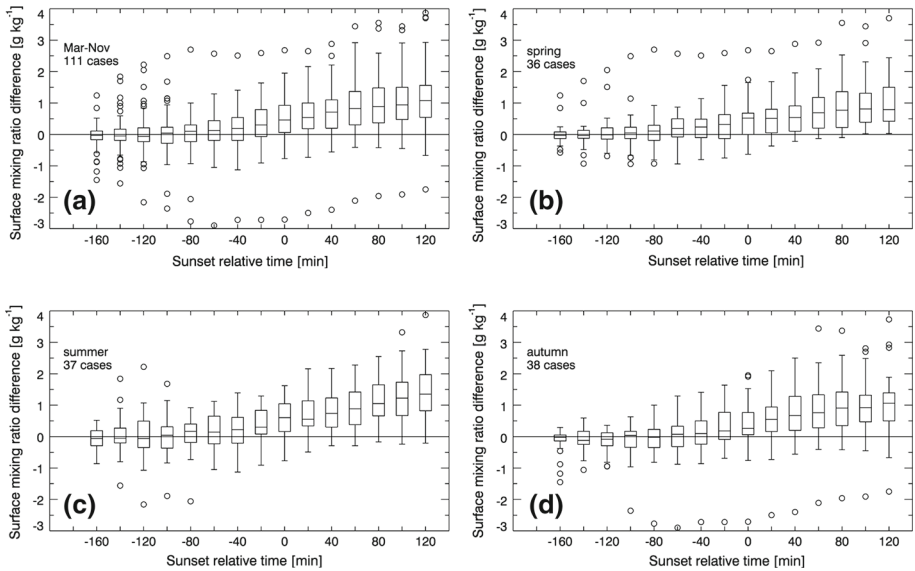


Fig. 4 As in Fig. 3, except for surface (2 m) water vapour mixing ratio difference (from the 3 h pre-sunset value) from the MIPS MPR, with a reference line at 0.0

Figure 4 shows the quartile analysis for values of the 15-min mean surface r_v difference from the 3-h pre-sunset value obtained from the MPR. Across all three seasons considered (Fig. 4a), the mean r_v steadily increases, ending 12% (1 g kg^{-1}) higher at 2 h after sunset than at 3 h before sunset. The increase trend appears to initiate after 80 min pre-sunset. This

trend is consistent among each season, though it starts nearly 1 h earlier in spring (Table S1). The size of the range of observed r_v difference values appears to vary slightly with time of year: summer events exhibit the smallest overall range and fewest outliers, while the range shows a greater increase with time during spring and autumn transitions. Increases in the r_v difference are largest in the summer case group, with the median value reaching about 1.3 g kg^{-1} , while in the spring and autumn it achieves about 0.7 and 1.1 g kg^{-1} , respectively. Autumn (spring) events account for the majority of the negative (positive) outlier cases in the full March–November group. Normalized r_v values (Fig. S2 in the Supplementary material) show similar trends, with a narrower range in summer due to the generally higher initial values typical of summertime in Alabama.

We note that sharp increases or “jumps” in r_v do occur in most of the individual cases, in line with the findings of previous investigators; however, applying the 15-min mean often smoothes out these abrupt changes. Such signatures occur at a wide range (2+h) of sunset relative times, which is consistent with the time frames reported by [Busse and Knupp \(2012\)](#) for a smaller set of AET events at the same location. While they found the average sunset relative time for the initial r_v increase to be about 30 min in summer and a few minutes in autumn before sunset, the normalized r_v values in our investigation increase on average starting 80 min prior to sunset, with spring cases showing this start even 1 h earlier. This characteristic increase (often accomplished in the short-term “jumps”) in surface water vapour was highlighted by [Fitzjarrald and Lala \(1989\)](#) and [Acevedo and Fitzjarrald \(2001\)](#); both studies used autumn observations from the Hudson River valley in the vicinity of Albany, New York State, and the latter also found temporal variations in the start of the increase among various observational sites. As vertical mixing is effectively reduced by the decreasing surface heat flux and evaporation near the surface continues, a build up of r_v results that persists until eventual dew (or frost) formation later in the night. This upward trend in the mean r_v continues even after sunset, implying that evaporation is the main contributor to the increase, since transpiration from plants requires photosynthesis.

[Fitzjarrald and Lala \(1989\)](#) and the follow-up work of [Acevedo and Fitzjarrald \(2001\)](#) showed that near the time of maximum r_v increase an inflection point in the surface temperature trace often occurs. The former mention the contribution of the net radiation term to temperature tendency (and the saturation specific humidity budget) during the transition, and we reiterate here that our cases were intentionally selected to only include clear-sky or nearly clear-sky days. [Busse and Knupp \(2012\)](#) reported on this effect from the perspective of a vertical temperature difference between 2 m and 10 m, where this vertical temperature difference ($T_2 - T_{10}$) can be viewed as a proxy for the surface heat flux. We proceed likewise, and the means for each case group are presented in Fig. 5a. In all seasons, the initial mean $T_2 - T_{10}$ is roughly 0.8°C , in contrast to typical values as large as $2\text{--}3^\circ\text{C}$ around midday. A steady decrease occurs at sunset, and on average a shallow inversion forms by about 20 min prior to sunset, with summer transitions showing a slight delay relative to other seasons in this change of sign. The strength of this early inversion increases after sunset, but the rate of increase slows down by about 1 h post-sunset when $T_2 - T_{10}$ changes little in the mean for all seasons. The average behaviour of this difference is similar across the seasons: the autumn transition ends the 5-h period with the largest magnitude difference (-0.43°C), and spring events show a value of -0.38°C (difference within the measurement error). Summer events are distinguished from the equinox seasons, with an overall smaller final value of $T_2 - T_{10}$ (only -0.21°C).

[Busse and Knupp \(2012\)](#) showed early inversion formation on average 15 min before sunset in the summer and 8 min before sunset in the autumn, with their autumn events expressing a stronger vertical temperature gradient at the end of the afternoon-to-evening

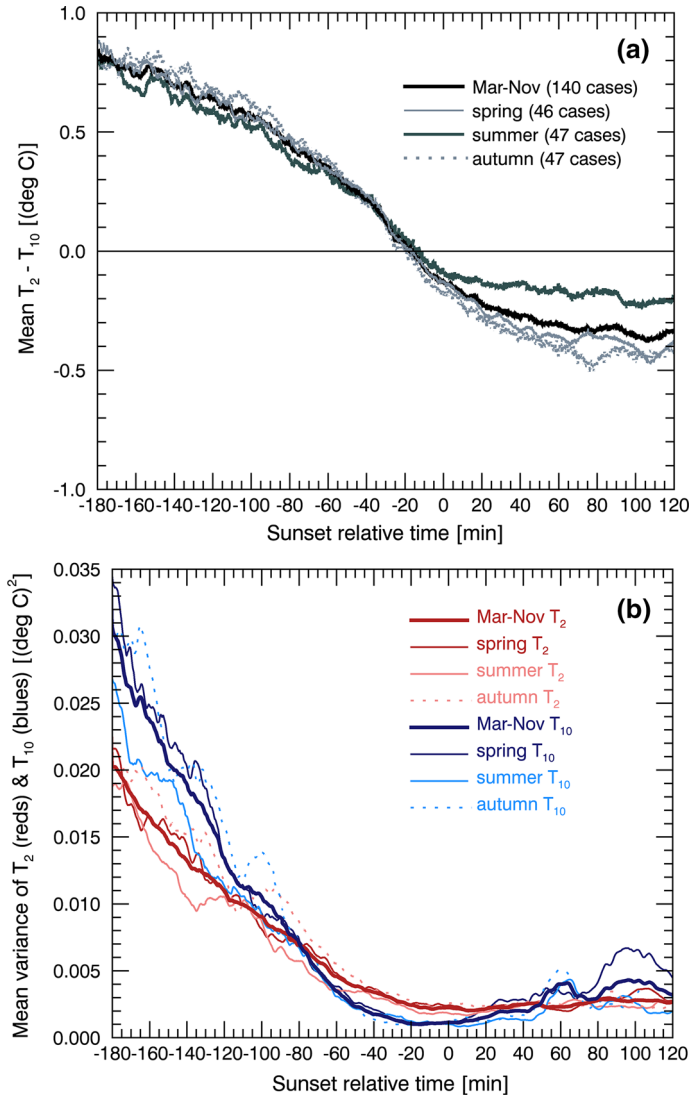


Fig. 5 As in Fig. 2, except for **a** temperature difference ($T_2 - T_{10}$) and **b** temperature variance about 15-min mean at 2 m (reds) and 10 m (blues)

transition. Our results show the initial inversion forming slightly earlier (about 20 min before sunset), especially with the inclusion of the spring season, and on average the late AET $T_2 - T_{10}$ difference for our equinox season cases is about twice that found in summertime. The faster cooling in the spring and autumn is likely due to a combination of the greater total daily insolation and higher precipitable water amounts that alter the surface radiative balance in summer months. If a transition event does not form an initial inversion it is most likely to be a summer case, again consistent with Busse and Knupp (2012). There is a hint, in the mean, of spring and summer events evolving towards a quasi step-like pattern, similar to that shown for the horizontal wind-speed variance for those seasons. However, the $T_2 - T_{10}$ steps

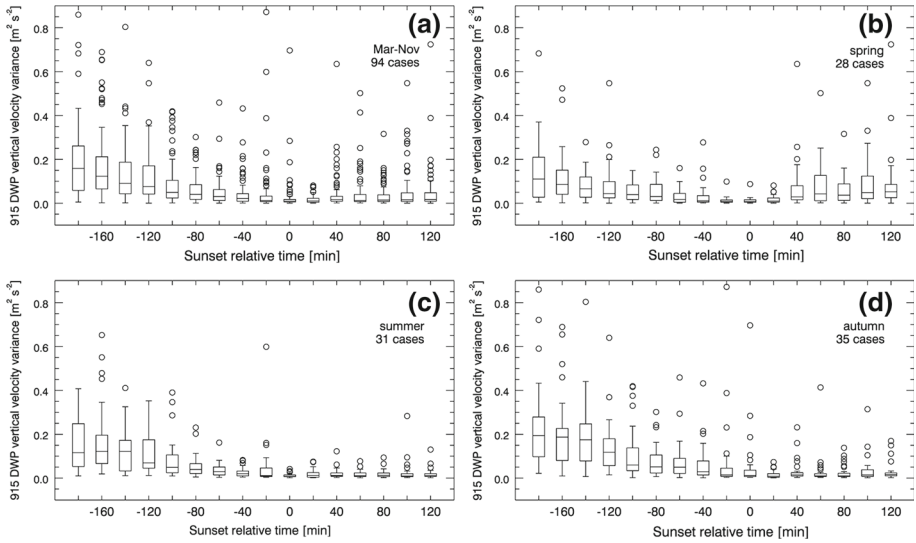


Fig. 6 As in Fig. 3, except for MIPS 915 DWP vertical motion variance at 200 m

for spring and summer (at about 120 min and 150 min pre-sunset, respectively) occur slightly ahead of the sharper $\overline{U^2}$ decline. A sharper decline in the temperature difference before the accelerated decrease of $\overline{U^2}$ suggests a decrease in buoyant production before a decrease in shear production of TKE with the convective regime of the PBL wanes. The decrease in buoyancy indicated by the temperature differences is also consistent with the rapid decrease in vertical motion variance (shown below).

Figure 5b depicts the change in temperature variance at these heights. On average, the variance of T_{10} is initially higher than that at 2 m, with spring cases showing the largest difference between the two heights. For the first 2 h of the AET period, the mean variance of T_{10} decreases at a faster rate than the mean variance of T_2 , and may be another indication of decreased vertical mixing during the transition, with the temperature fluctuations decreasing more rapidly at a greater height. Less variability in temperatures is also aligned with the occurrence of the sodar minimum reported by Busse and Knupp (2012). Variances at both heights become fairly steady near their minimum values by about sunset (20 min pre-sunset) for T_2 (T_{10}). After sunset, the temperature variance at both heights begins to increase, but much more slowly than the rate of decrease seen at the early part of the afternoon-to-evening transition. This modest increase is most pronounced at 10 m in the spring transitions, and we note that an increase in the temperature variance at both heights toward the end of the AET time frame is consistent with Busse and Knupp (2012). In order to capture truly representative temperature variance, faster response sensors are required, so these results should be taken in the context of the relatively long effective response time of the available sensors.

3.2 Vertical Motions

To complement $\overline{U^2}$ presented above, observations from the 915 DWP and DWL are used to obtain the vertical motion variance, and the vertical spatial and temporal resolutions of each of these platforms are included in Table 1. Figure 6 shows the quartile analysis of the vertical motion variance at 200 m as seen from the 915 DWP (w_{915}^2). While there are many outlier

cases (circles), the bulk of the values follow a clear decreasing trend. Grouped together, all observed transitions show a minimum in the range of the middle 50% (inner quartile range on the plot) of individual case values at the time of sunset. The range minimum occurs at the next time bin, 20 min after sunset, only for the autumn group (Fig. 6d). In the group of all cases, this range increases with time after sunset, primarily due to spring transitions (Fig. 6b) that show a sharply increased range at 40 min post-sunset and later. Autumn events also have a slight increase in range at the 100 min post-sunset time bin. In the mean values there is a similar pattern: spring cases exhibit an increase starting at the sunset +40 min bin (from 0.02 to $0.08 \text{ m}^2 \text{ s}^{-2}$), autumn events increase more modestly after sunset (0.01 – $0.03 \text{ m}^2 \text{ s}^{-2}$), and summer transitions show little range in the mean values after sunset (steady at about $0.02 \text{ m}^2 \text{ s}^{-2}$, see Table S1).

Because the DWL was newly acquired in 2013, data are only available for summer and autumn of that year. Figure 7 presents the quartile analysis for the DWL vertical motion variance ($\overline{w_{\text{DWL}}^2}$) at the 195-m gate. Both the magnitude and range of $\overline{w_{\text{DWL}}^2}$ increase between the first two time bins, and afterwards an overall decline begins and by sunset the mean value is below $0.01 \text{ m}^2 \text{ s}^{-2}$. Magnitudes and ranges remain small through the rest of the period in all cases. There is no suggestion of the post-sunset increase seen in $\overline{w_{915}^2}$. This is most likely a result of the 915 DWP's sensitivity to particulate scattering and the increased presence of insects and birds later in the evening, and its prominence in the spring could be attributed to greater migration activity. The DWL is not susceptible to this contamination, as discussed in more detail below. Numerical simulations of the AET time frame indicate differing rates of decay for horizontal and vertical velocity fluctuations (e.g. Nieuwstadt and Brost 1986; Pino et al. 2006). Our observations show a pattern consistent with these findings, with the vertical velocity variance of both platforms depicting a generally more rapid decline than occurs in the decline of $\overline{U^2}$, decreasing most rapidly within the 30 min before sunset (most evident in $\overline{w_{\text{DWL}}^2}$). That vertical motion fluctuations wane ahead of the horizontal fluctuations suggests that buoyancy driving the convective regime of the PBL diminishes first, and with less vertical mixing and turbulent transport contributions, $\overline{U^2}$ then also decays.

As mentioned above, previous work has indicated a potential for increases to existing horizontal wind convergence atop the surface layer during the AET period, and a resulting enhancement effect on existing convective elements (Jones and Bannon 2002; Murphey et al. 2006; Bluestein 2008). To help address this possibility, we consider the mean vertical motion, profile of horizontal wind magnitude, and radar-derived meso- γ scale convergence for the clear-sky, light wind conditions that best display the hallmark signatures of the afternoon-to-evening transition.

Fifteen-min mean values of DWL vertical motion (w_{DWL}) for all available cases are set in the sunset relative time frame and averaged at every vertical gate (30 m in length). The result, shown in Fig. 8, is a composite sunset relative time-height view of mean w_{DWL} . Early in the AET period, upward motion extends through the majority of the PBL. Coherent towers at 3 h before sunset indicate there is still positively buoyant thermal activity early in the studied time frame. This is corroborated by the increase in the 195-m $\overline{w_{\text{DWL}}^2}$ seen for the 160-min pre-sunset time bin (Fig. 7). As each component of TKE (in analogue here as $\overline{U^2}$ and $\overline{w_{\text{DWL}}^2}$) decreases, evidence of thermals diminishes and a persistent layer of upward motion forms by about 1 h before sunset. Weaker downward motion begins to dominate at heights above 500 m and below 200 m.

The roughly 200-m thick layer of relatively strong upward motion centred at about 300 m forms by 1 h before sunset and persists through the remainder of the AET period. This structure is evident in all available cases. When this layer initially forms, the final coherent column

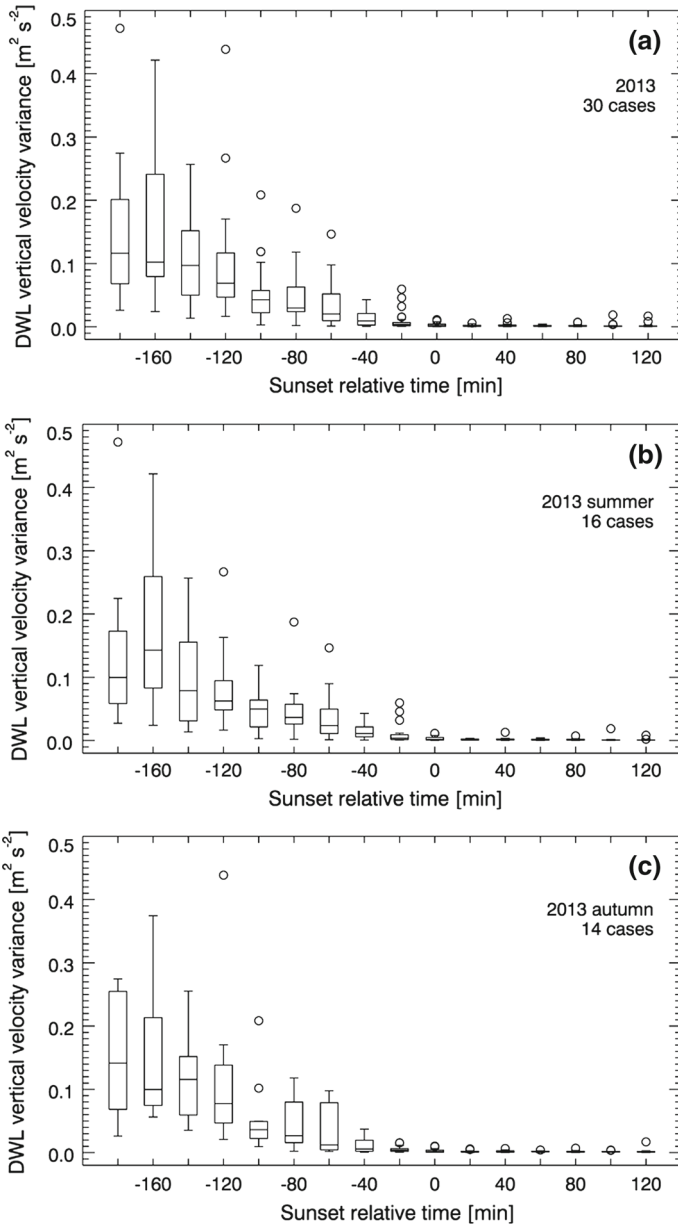


Fig. 7 As in Fig. 3, except for DWL vertical motion variance at 195 m for (a) all available cases. Because it was newly acquired in spring 2013, the DWL is only available for some (b) summer and (c) autumn 2013 events

of positive w_{DWL} occurs, and for summer cases this column extends above 1 km while for autumn cases it reaches about 800 m. That summer cases display a stronger convective regime early in the afternoon-to-evening transition and more vigorous final column of positive w_{DWL} may be a result of stronger thermals due to greater insolation in summer. Peak magnitudes of the composite mean w_{DWL} in the persistent layer occur just after it forms ($0.2\text{--}0.25 \text{ m s}^{-1}$).

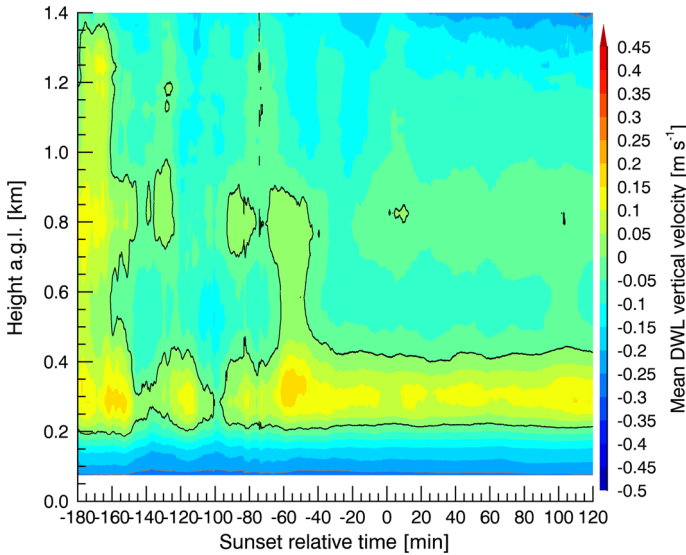


Fig. 8 Composite sunset relative time-height of DWL 15-min mean vertical motion for all 30 available 2013 cases, with the zero contour shown in black

Another interesting finding from the DWL data is the persistence of downward motion below 200 m, noting that the minimum range for the instrument is 75 m (Table 1). Time-height sections of mean w_{DWL} extending to dawn show that both the positive and negative vertical motion layers are prevalent through the night (not shown) and occur regardless of the low-level mean wind. We believe both of these layers are at least in part manifestations of local effects. While the upward motion layer may include a transition effect, its persistence through the overnight hours suggests a stronger local effect, possibly a remnant warm plume atop the relatively warmer building and more urbanized area around the campus (see Fig. 1). The endurance of the downward motion below about 200 m is likely due to downslope flow in the area, predominantly due to elevated terrain surrounding the site (most notably the Monte Sano area to the east and south of the MIPS, approximated by the forested regions indicated in Fig. 1). As the DWL is a new addition to the UAH observation suite, efforts are underway to better understand these local effects.

Composites of sunset-relative 15-min mean w_{915} for all the available cases are given in Fig. 9. Values for days when the 915 DWP operated in different modes are interpolated to the coarsest vertical gate spacing the 915 DWP used across all cases (106 m, as noted in the previous section and Table 1) so that the composite plots utilize consistent dimensions for all cases. From the perspective of the 915 DWP, the most striking feature of the transition is a vertically coherent maximum in upward motion focused at about 35 min post-sunset. The peak mean w_{915} in this tower-like structure is about 0.6 m s^{-1} centred at about 800 m in the composite of all cases (Fig. 9a). Summer cases (Fig. 9c) exhibit the least prominent upward motion tower of the three seasons, and summer is the only season to show a recurrence of consistent downward mean w_{915} below 1 km sometime after sunset. In general, peak composite mean magnitudes of w_{915} are about twice as large as those of w_{DWL} .

It is important to view Figs. 6, 7, 8, 9 in the context of the operation of the instruments. The 915 DWP uses a 0.33-m wavelength sensitive to Bragg and particulate scattering (from biota and lofted particles) within the sample volume (9° by 60 or 106 m thick). Insects are widely

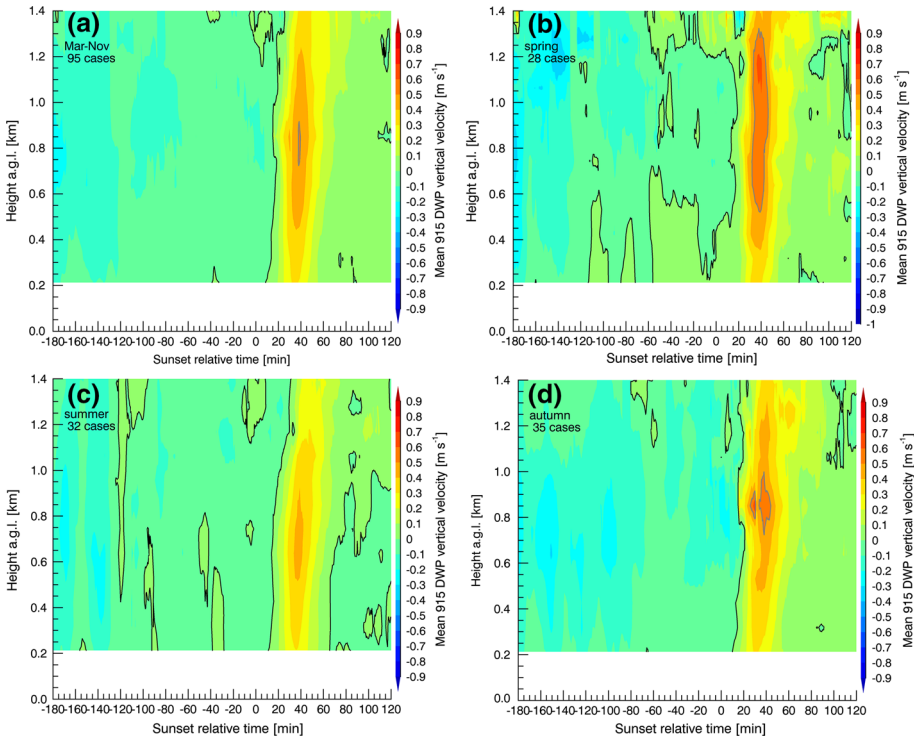


Fig. 9 Composite sunset relative time-height of MIPS 915 DWP 15-min mean vertical motion for all available cases (a) and by season (b–d), with the 0 m s^{-1} (0.5 m s^{-1}) contour shown in black (grey)

acknowledged as the main generator of clear-air radar return in the PBL, and birds can also contaminate radar velocities (e.g. Wilson et al. 1994; Martin and Shapiro 2007). Angevine (1997) reports a downward bias in mean UHF profiler vertical velocities up to 0.3 m s^{-1} in the daytime PBL due to the subsidence of particulate scatterers, and Geerts and Miao 2005 show that insects can actively oppose PBL upward vertical motions. Concentration of insects in the southern Plains peaks in the mid-afternoon and overnight, with minima near sunrise and dusk (Martin and Shapiro 2007). We estimate a similar diurnal insect pattern at our study location, based on informal inspection of ARMOR dual-polarimetric data over several years. The tower-like structure of enhanced upward motion seen in composite mean w_{915} and the increased range of w_{915}^2 after sunset (Fig. 6) are probably manifestations of emerging insects (after the dusk minimum and in advance of the nocturnal maximum) and the take off of migratory birds, the latter being most prominent in the equinox seasons. Potential variations in the migration schedules of bird species may help explain the differences between the spring and autumn results. In contrast to the 915 DWP, the DWL collects measurements over a miniscule volume, utilizes a short wavelength of $1.5\text{ }\mu\text{m}$ that is sensitive to aerosol backscatter, and has a very stable transceiver, all of which provide for very accurate velocity measurements (Pearson et al. 2009). Therefore, we consider the w_{DWL} data to be a true representation of the flow velocity, while the w_{915} values represent the net result of multiple scattering effects. Wind profilers akin to the MIPS 915 DWP have been used extensively in PBL field studies, and we believe our results are instructive in illustrating the importance of

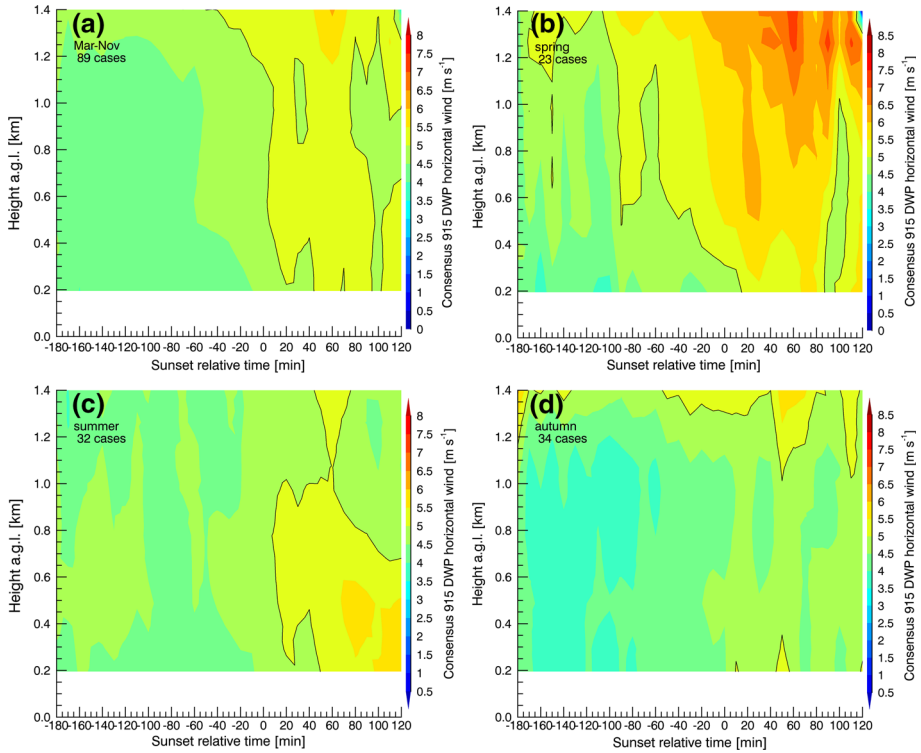


Fig. 10 Composite sunset relative time-height of MIPS 915 DWP 10-min consensus horizontal wind magnitude for all available cases (a) and by season (b–d), with the 5 m s^{-1} contour shown in black

being mindful of the scattering mechanisms that an observation platform employs. Vertical velocity fluctuations and composite mean w_{DWL} show a more realistic depiction of typical vertical air motions during the AET time frame, though at the observation site there are evidently local, low-level effects in the mean.

3.3 Horizontal Wind Speed and Convergence

Considering changes in the horizontal wind profile, a composite analysis is presented in Fig. 10 for the 915 DWP 10-min consensus horizontal wind speed (\bar{U}). When all available cases are averaged (Fig. 10a), a modest increase occurs at most heights, with winds at 300 m initially between 4 and 4.5 m s^{-1} and up to 5.5 m s^{-1} by 20 min post-sunset. Spring events (Fig. 10b) show the strongest increase in \bar{U} . At 300 m, initial values range from about 3.5 to 4.5 m s^{-1} , and at 20 min post-sunset the composite average reaches 5.5 m s^{-1} . Higher in the PBL, spring cases show a striking increase, with wind speeds exceeding 6 m s^{-1} above 500 m prevalent after 20 min post-sunset. This suggests elevated wind-speed shear across the PBL in spring that may partially account for a modest increase in near-surface variability, most evident in the T_{10} variance (Fig. 5b) towards the end of the time period. Composites of the observed summer and autumn cases show more variability: summer events (Fig. 10c) show peak composite values that extend up to 600 m after 70 min post-sunset. Autumn cases (Fig. 10d) display overall smaller \bar{U} early in the afternoon-to-evening transition, but

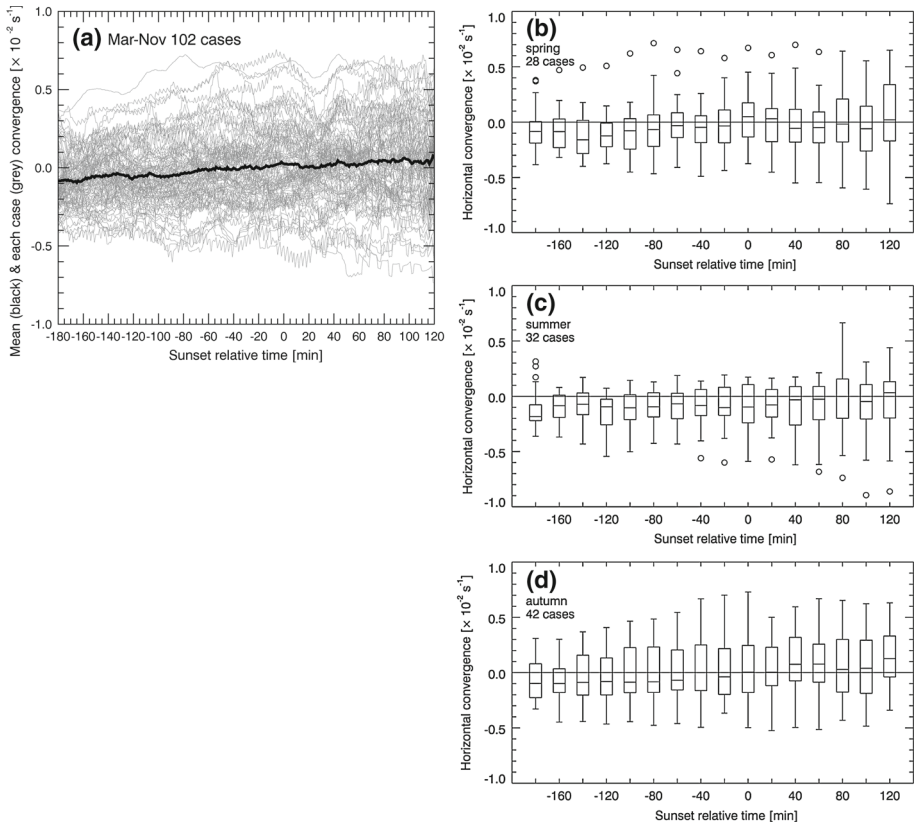


Fig. 11 a 10-km EVAD horizontal wind convergence at 300 m a.g.l. mean (*black*) and all available cases (*grey*). **b–d** Quartile analysis as in Fig. 3 by season, with a reference line at 0.0

an increase across the 5-h time period is evident, with an isolated peak of about 5 m s^{-1} at 50 min post-sunset. There is also a slight increase at the higher levels in autumn, but this is much smaller than that seen in spring. Enhanced magnitudes in the equinox seasons may include a possible contamination due to migrating biota that tend to fly with the wind, and may impart an additional component to the velocity. Summer has a decreased likelihood of migration activity (i.e., more random flight directions of biota are more likely), thus it is possible our summer results here are more robust. The increase in mean horizontal wind speed observed above the surface layer during the transition may play a role in enhancing existing horizontal wind convergence, as found along boundaries such as drylines, and could promote the invigoration of convective elements, similar to that shown by Jones and Bannon (2002) and Murphey et al. (2006).

To broaden our study beyond point and profile measurements, horizontal wind convergence derived using a 10-km radius EVAD circle is computed for cases with available ARMOR radar data (102 of the 143 total cases). Figure 11a shows the convergence values at 300 m in the sunset relative time frame for all cases. There is a slight upward trend in the mean of all cases, but not all individual events depict a steady increase, or even any increase. Also evident is a nearly symmetric grouping of both positive and negative (divergence) values at all times. This can be seen in the quartile analysis from each season (Fig. 11b–d) as well. Within the

10-km radius of ARMOR used in the EVAD computations, there are several surface features worth noting (Fig. 1). Portions of the southern extent of the Tennessee River straddle the effective location of the EVAD circle. Along the eastern and north-eastern regions there are discontinuities from more urban areas against residential and wooded wetland-type areas. To the west and south-west of ARMOR, agricultural lands dominate. It is possible for these differing surface qualities to establish fine scale variations in temperature and moisture (e.g. along edges of irrigated agricultural areas adjacent to more urban areas, see Fig. 1) capable of inducing localized solenoidal circulations along the edges of the EVAD radius. For example, Asefi-Najafabady et al. (2010) describe the development of a local lake-breeze circulation that regularly occurs along the lake 20 km west of ARMOR. Such localized features may partially account for the nearly symmetric range in convergence values found, but further investigation would be required to state this definitively.

All seasons display a large range of horizontal wind convergence values at each sunset relative time. Each season shows a modest upward trend in median values, but the range is broad. In fact, the lowest individual values at each time interval show a *decrease* in convergence (increasing divergence) after sunset for both the spring and summer case groups. Case selection criteria may help account for this: cases are similar on the synoptic scale with high pressure over northern Alabama. This lends an expectation for low-level horizontal wind divergence to be common among the cases, and Fig. 11 shows that indeed the majority of the cases start the AET period with negative convergence values. If no change occurs to the wind field orientation (i.e., no significant change to the direction of the flow), and the horizontal wind speed increases (as Fig. 10 indicates), then it is reasonable to expect increased divergence above the surface layer, contributing to the apparent symmetry of Fig. 11. Still, in the mean a steady convergence increase from $-0.85 \times 10^{-3} \text{ s}^{-1}$ at 3 h before sunset to $+0.69 \times 10^{-3} \text{ s}^{-1}$ at 2 h after sunset occurs and is statistically significant at the 0.01 probability value. This signature may relate to an increase in pre-existing low-level convergence along drylines shown by Jones and Bannon (2002) and could act in specific circumstances to aid in convective initiation or enhancement, akin to the Murphey et al. (2006) case study.

3.4 Summary

Our investigation of the afternoon-to-evening transition reveals several signatures of the transition, many of which have been noted in previous studies using a smaller number of cases, different locations, and numerical simulations. A visual summary of the signatures observed in this study is given in Fig. 12, which shows the average sunset relative time of each indicator. It should be noted that the order of events presented in Fig. 12 depicts the transition from multiple perspectives in the average sense, i.e., not every individual case follows the same order of signature occurrence, and in some cases not all signatures are present (e.g. early inversion formation does not always occur).

Our results depict an abrupt decrease in turbulent quantities during the transition, consistent with previous studies. Surface measurements show the characteristic decrease in wind speed, temperature variance, and vertical temperature gradient. An increase in mean r_v across the afternoon-to-evening transition is observed for nearly all cases, while equinox seasons display a slightly smaller absolute increase than in summer. Vertical motion measured by the 915 DWP and DWL shows different behaviour during the transition due to the scattering regime each employs and the 915 DWP's sensitivity to biological targets. The DWL presents a more realistic depiction of the vertical motion, and indicates an enduring minimum in vertical motion variance after sunset and a persistent layer at 200–400 m a.g.l. of weak ($0.2\text{--}0.25 \text{ m s}^{-1}$) mean upward motion that forms by about 1 h prior to sunset. A column

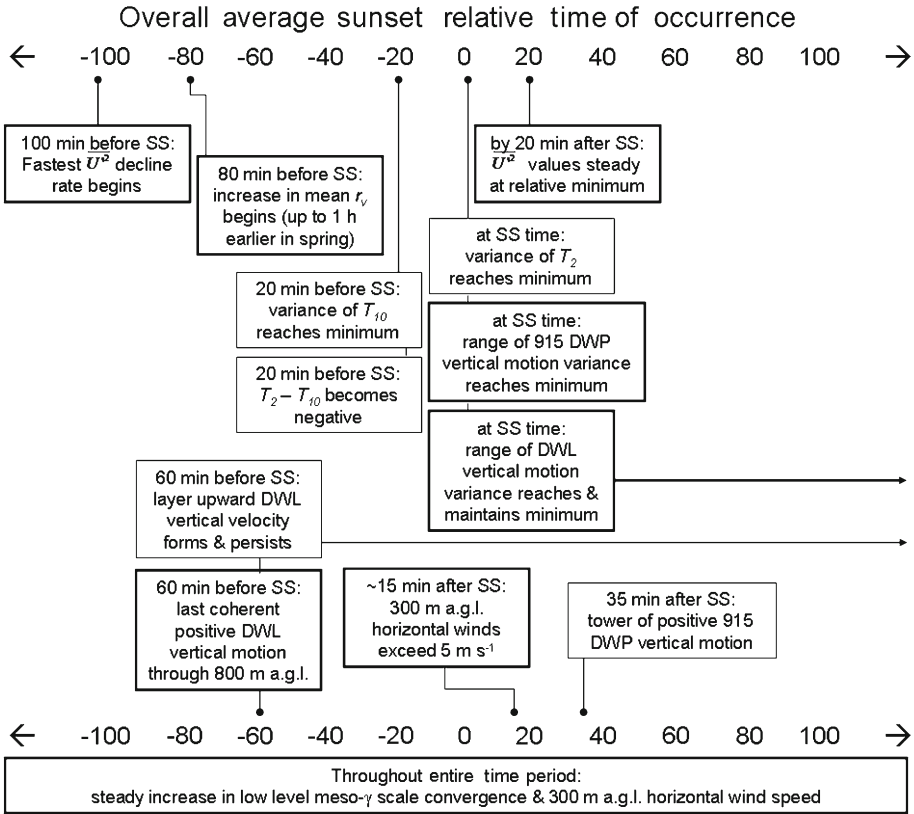


Fig. 12 Visual summary of average sunset (SS) relative time for observed AET signatures. Items with *bold boxes* occur most consistently in our results, while *thinner boxes* indicate signatures that are strong in the mean but do not necessarily occur in each case

of weaker (but still positive) values extending to at least 800 m lasting for about 20 min coincides with the formation of this layer. We note that the layer of upward motion may be due in part to localized effects. Profiles of horizontal wind speed obtained from the 915 DWP show a steady, modest increase at low-levels across the AET period. At 300 m, spring events show the largest increase (about 2 m s^{-1} in the mean). There is also a gradual, notable increase in meso- γ scale horizontal wind convergence above the surface layer (300 m) across the transition. However, there is substantial range in the convergence results, with a nearly symmetric pattern of both positive and negative (divergence) values occurring at all sunset relative times in each of the three seasons considered.

A comparison of the normalized mean wind and temperature variances for all available cases is presented in Fig. 13 on a logarithmic scale. Vertical velocity fluctuations decay more rapidly than those in the horizontal, consistent with numerical simulations. In fact, by the time the normalized horizontal wind variance has been halved, the normalized vertical wind variance has decayed to nearly a tenth of its initial value. Temperature fluctuations at 10 m decrease more rapidly than at 2 m, and their sharper decline tends to precede more rapid vertical velocity variance decay, especially at about 130 min and 90 min prior to sunset. This suggests the reduced buoyantly-driven thermals inhibits vertical mixing, and can be regarded

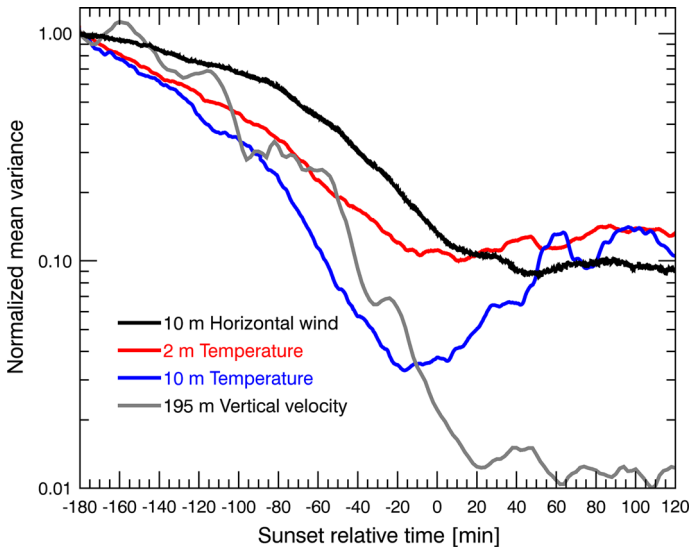


Fig. 13 Comparison of normalized variances on a logarithmic scale. Each curve represents the mean value of all available cases, normalized by the value at 3 h prior to sunset. Surface data used for the horizontal wind and both temperature curves is from 140 AET events, while the vertical velocity curve is comprised of the 30 cases with DWL observations

as the effect of a rapidly decreasing buoyancy term (becoming a loss term) in the vertical velocity variance budget equation. As the vertical wind variance diminishes more rapidly, $\overline{U'^2}$ decreases in response to lessened vertical and turbulent transport of momentum, and this decrease is slower than in the vertical as the mechanical production continues to serve as a source term. After the declines in these turbulent quantities have occurred, an increase in horizontal wind speed is evident in the composite mean (Figs. 10, 12), with the fastest rate of increase occurring between sunset ± 20 min, consistent with the average time when $\overline{U'^2}$ and w_{DWL}^2 achieve minimum values. As turbulent motions in the PBL decay, we expect the wind speed above the surface layer to increase, and as a result potentially enhance any pre-existing low-level horizontal convergence supportive of modest upward velocity.

Finally, we mention that the present results are valid for the site and seasons observed. Many investigators have noted that terrain and surface feature variations (such as land use or type) can influence how the PBL progresses from its daytime regime to the more stable nocturnal regime (Caughey et al. 1979; Acevedo and Fitzjarrald 2001; Brazel et al. 2005). Based on such studies, it would be reasonable to expect less variability in timing of each AET signature for a more homogeneous location, while more heterogeneous and topographically diverse areas could expect more complicated, and perhaps longer lasting, transition periods. For example, effects due to topographic phenomena, downslope and return flows, and potential urban heat-island effects have been shown to cause considerable variability in the AET pattern over the complex surface features of the Phoenix area (Brazel et al. 2005).

4 Conclusions

We have presented an investigation of the PBL's afternoon-to-evening transition (AET) under clear-air conditions for three seasons in Huntsville, Alabama, in the south-eastern USA, that

adds to the relative paucity of long term, multi-platform datasets for the transition time period (defined herein as 3 h before to 2 h after sunset). Several signatures of the transition are identified and show trends that are generally consistent with previous work. In the hours approaching sunset, turbulent quantities such as the horizontal wind variance (10 m) and temperature variance (2 and 10 m) monotonically decrease as surface heating diminishes. A steady increase in r_v (2 m) begins at 80 min before sunset, though the spring transition commences this rise about 1 h earlier. Initial inversion formation takes place by 20 min pre-sunset, and variances in temperature at both 2 m and 10 m achieve minimum values within the same time. Overall, the vertical velocity variance at about 200 m measured from both the 915 DWP and DWL reaches a minimum range at about the time of sunset. The DWL, which better represents true air motion, shows this minimum remains up at least 2 h after sunset. Distinctly different structures in the profiles of mean vertical velocity from the 915 DWP and DWL are likely due to the summation of Bragg scattering and particulate biological target effects on the vertical motion obtained by the radar.

Results show a consistent pattern in the timing of the decline of turbulent parameters near the surface and at 200 m and an increase in the horizontal wind speed and magnitude of meso- γ scale convergence at 300 m. In general, temperature variances (first at 10 m, then at 2 m) decrease slowly, then more quickly after about 90 min pre-sunset. This is preceded by the decay of vertical velocity fluctuations as thermal activity becomes less vigorous. After the decline of the vertical wind variance steepens, the decrease in the horizontal wind fluctuations also accelerates, and finally a modest increase in the mean horizontal wind speed occurs just above the surface layer. Maximum horizontal winds at 300 m occur after about 15 min post-sunset, with a steady rise evident through the transition. Radar-derived horizontal wind convergence values show considerable range, but in the mean increase across the full AET period (effectively about $0.3 \times 10^{-3} \text{ s}^{-1} \text{ h}^{-1}$). In the presence of an existing convergence feature, the gradual increase in the flow atop the surface layer could aid a parcel's ability to reach its level of condensation or free convection. While it is impossible to say this study confirms the diurnal dryline process examined by Jones and Bannon (2002) as a mechanism for the delay in convective initiation along an existing boundary until the afternoon-to-evening transition, our observations indicate the plausibility of a generalized low-level convergence enhancement resulting from AET effects. Related ongoing work includes multi-platform observational analysis and numerical simulation of observed AET convective enhancement and initiation case studies along pre-existing boundaries.

Acknowledgments Discussions with David Bowdle were helpful in interpreting the DWL observations. We are also thankful to three reviewers whose comments greatly improved this manuscript. This work was supported by the National Science Foundation under Grant AGS-1110622.

Open Access This article is distributed under the terms of the Creative Commons Attribution License which permits any use, distribution, and reproduction in any medium, provided the original author(s) and the source are credited.

References

- Acevedo OC, Fitzjarrald DR (2001) The early evening surface-layer transition: temporal and spatial variability. *J Atmos Sci* 58:2650–2667
- Angevine WM (1997) Errors in mean vertical velocities measured by boundary layer wind profilers. *J Atmos Ocean Technol* 14:565–569
- Angevine WM (2008) Transitional, entraining, cloudy, and coastal boundary layers. *Acta Geophys* 56:2–20

- Asefi-Najafabady S, Knupp K, Nair U, Mecikalski J, Welch R (2010) Ground-based measurements and Dual-Doppler analysis of 3D wind fields and atmospheric circulations induced by a meso- γ scale inland lake. *J Geophys Res* 115:D23117
- Beare RJ, Edwards JM, Lapworth AJ (2006) Simulation of the observed evening transition and nocturnal boundary layers: large-eddy simulation. *Q J R Meteorol Soc* 132:81–99
- Bennett LJ, Weckwerth TM, Blyth AM, Geerts B, Miao Q, Richardson YP (2010) Observations of the evolution of the nocturnal and convective boundary layers and the structure of open-celled convection on 14 June 2002. *Mon Weather Rev* 138:2589–2607
- Bianco L, Gottas D, Wilczak JM (2013) Implementation of a Gabor transform data quality-control algorithm for UHF wind profiling radars. *J Atmos Ocean Technol* 30:2697–2703
- Bluestein HB (2008) Surface boundaries of the southern plains: their role in the initiation of convective storms. *Meteorol Monogr* 33:5–34
- Bonin T, Chilson P, Zielke B (2013) Observations of the early evening boundary-layer transition using a small unmanned aerial system. *Boundary-Layer Meteorol* 146:119–132
- Brazel AJ, Fernando HJS, Hunt JCR, Selover N, Hedquist BC, Pardyjak E (2005) Evening transition observations in Phoenix, Arizona. *J Appl Meteorol* 44:99–112
- Busse J, Knupp K (2012) Observed characteristics of the Afternoon-Evening boundary layer transition based on sodar and surface data. *J Appl Meteorol Climatol* 51:571–582
- Caughey SJ, Wyngaard JC, Kaimal JC (1979) Turbulence in the evolving stable boundary-layer. *J Atmos Sci* 36:1041–1052
- Comman LB, Goodrich RK, Morse CS, Ecklund WL (1998) A fuzzy logic method for improved moment estimation from Doppler spectra. *J Atmos Ocean Technol* 15:1287–1305
- Dixon M (2010) Radx C++ Software. http://ral.ucar.edu/projects/titan/docs/radial_formats/radx.html
- Edwards JM, Beare RJ, Lapworth AJ (2006) Simulation of the observed evening transition and nocturnal boundary layers: single-column modeling. *Q J R Meteorol Soc* 132:61–80
- Fitzjarrald DR, Lala GG (1989) Hudson valley fog environments. *J Appl Meteorol* 28:1303–1328
- Fry J, Xian G, Jin S, Dewitz J, Homer C, Yang L, Barnes C, Herold N, Wickham J (2011) Completion of the 2006 National Land Cover Database for the conterminous United States. *Photogramm Eng Remote Sens* 77(9):858–864
- Geerts B, Miao Q (2005) The use of millimeter Doppler radar echoes to estimate vertical air velocities in the fair-weather convective boundary layer. *J Atmos Ocean Technol* 22:225–246
- Grant AM (1997) An observational study of the evening transition boundary-layer. *Q J R Meteorol Soc* 123:657–677
- Grimsdell AW, Angevine WM (2002) Observations of the afternoon transition of the convective boundary layer. *J Appl Meteorol* 41:3–11
- Holtstlag AAM, Svensson G, Baas P, Basu S, Beare B, Beljaars ACM, Bosveld FC, Cuxart J, Lindvall J, Steeneveld GJ, Tjernström M, Van De Wiel BJH (2013) Stable atmospheric boundary layers and diurnal cycles: challenges for weather and climate models. *Bull Am Meteorol Soc* 94:1691–1706
- Jones PA, Bannon PR (2002) A mixed-layer model of the diurnal dryline. *J Atmos Sci* 59:2582–2593
- Karan H, Knupp K (2006) Mobile Integrated Profiler System (MIPS) observations of low-level convergent boundaries during IHOP. *Mon Weather Rev* 134:92–112
- Knupp KR, Coleman T, Phillips D, Ware R, Cimini D, Vandenberghe F, Vivekanandan J, Westwater V (2009) Ground-based passive microwave profiling during dynamic weather conditions. *J Atmos Ocean Technol* 26:1057–1073
- Lothon M, Lohou F, Pino D, Couvreux F, Pardyjak ER, Reuder J, Durand P, Hartogensis O, Legain D, Augustin P, Gioli B, Faloona I, Yagüe C, Alexander DC, Angevine WM, Bargain E, Barrié J, Bazile E, Bezombes Y, Blay-Carreras E, van de Boer A, Boichard JL, Bourdon A, Butet A, Campistron B, de Coster O, Cuxart J, Dabas A, Darbieu C, Deboudt K, Delbarre H, Derrien S, Flament P, Fourmentin M, Garai A, Gibert F, Graf A, Groebner J, Guichard F, Jonassen M, van den Kroonenberg A, Lenschow DH, Magliulo V, Martin S, Martinez D, Mastrorillo L, Moene AF, Molinos F, Moulin E, Pietersen HP, Pignatelli B, Pique E, Román-Cascón C, Rufin-Soler C, Saïd F, Sastre-Marugán M, Seity Y, Steeneveld GJ, Toscano P, Traullé O, Tzanos D, Wacker S, Wildmann N, Zaldei A (2014) The BLLAST field experiment: boundary-layer late afternoon and sunset turbulence. *Atmos Chem Phys Discuss* 14:10789–10852
- Mahrt L (1981) The early evening boundary layer transition. *Q J R Meteorol Soc* 107:329–343
- Martin WJ, Shapiro A (2007) Discrimination of bird and insect radar echoes in clear air using high-resolution radars. *J Atmos Ocean Technol* 24:1215–1230
- Matejka T, Srivastava RC (1991) An improved version of the Extended Velocity-Azimuth Display analysis of single-Doppler radar data. *J Atmos Ocean Technol* 8:453–466
- Morse CS, Goodrich RK, Cornman LB (2002) The NIMA method for improved moment estimation from Doppler spectra. *J Atmos Ocean Technol* 19:274–295

- Murphey HV, Wakimoto RM, Flamant C, Kingsmill DE (2006) Dryline on 19 June 2002 during IHOP. Part I: airborne Doppler and LEANDRE II analyses of the thin line structure and convection initiation. *Mon Weather Rev* 134:406–430
- Nadeau DF, Pardyjak ER, Higgins CW, Fernando HJS, Parlange MB (2011) A simple model for the afternoon and early evening decay of the convective turbulence over different land surfaces. *Boundary-Layer Meteorol* 141:301–324
- Nieuwstadt FTM, Brost RA (1986) The decay of convective turbulence. *J Atmos Sci* 43:532–546
- Oye R, Mueller C, Smith S (1995) Software for radar translation, visualization, editing, and interpolation. In: 27th Conference on radar meteorology. American Meteorological Society, Vail
- Pearson GN, Davies F, Collier C (2009) An analysis of the performance of the UFAM pulsed Doppler lidar for observing the boundary layer. *J Atmos Ocean Technol* 26:240–250
- Petersen WA, Knupp KR, Carey LD, Phillips D, Deierling W, Gatlin PN (2009) The UAH/NSSTC Advanced Radar for Meteorological and Operational Research (ARMOR). In: 34th Conference on radar meteorology. American Meteorological Society, Williamsburg
- Pino D, Jonker HJJ, de Arellano JVG, Dosio A (2006) Role of shear and the inversion strength during sunset turbulence over land: characteristic length scales. *Boundary-Layer Meteorol* 121:537–556
- Sorbjan Z (1997) Decay of convective turbulence revisited. *Boundary-Layer Meteorol* 82:501–515
- Stull RB (1988) An introduction to boundary layer meteorology. Kluwer, Dordrecht, 666 pp
- Wilson JW, Weckwerth TM, Vivekanandan J, Wakimoto RM, Russell RW (1994) Boundary layer clear-air radar echoes: origin of echoes and accuracy of derived winds. *J Atmos Ocean Technol* 11:1184–1206